

Modeling contamination migration on the Chandra X-ray Observatory

Stephen L. O'Dell^{*a}, Douglas A. Swartz^b,
Paul P. Plucinsky^c, Mark A. Freeman^c, Maxim L. Markevitch^c, Alexey A. Vikhlinin^c,
Kenny C. Chen^d, Rino J. Giordano^e, Perry J. Knollenberg^d, Peter A. Morris^d, Hien Tran^d,
Neil W. Tice^f, and Scot K. Anderson^g

^a NASA Marshall Space Flight Center, NSSTC/XD12, 320 Sparkman Dr., Huntsville, AL 35805

^b Universities Space Research Assoc., NSSTC/XD12, 320 Sparkman Dr., Huntsville, AL 35805

^c Harvard–Smithsonian Center for Astrophysics, CfA/MS70, 60 Garden St., Cambridge, MA 02138

^d Northrop Grumman Space Technology, NGST, One Space Park, Redondo Beach, CA 90278

^e Northrop Grumman Space Technology, CfA/MS33, 60 Garden St., Cambridge, MA 02138

^f Lockheed Martin, 8391 W. Nichols Ave., Littleton, CO 80128

^g Lockheed Martin, 13528 Elsie Rd., Conifer, CO 80433

ABSTRACT

During its first 6 years of operation, the cold (-60°C) optical blocking filter of the Advanced CCD Imaging Spectrometer (ACIS), on board the *Chandra X-ray Observatory*, has accumulated a contaminating layer that attenuates the low-energy x rays. To assist in assessing the likelihood of successfully baking off the contaminant, members of the *Chandra* team developed contamination-migration simulation software. The simulation follows deposition onto and (temperature-dependent) vaporization from surfaces comprising a geometric model of the Observatory. A separate thermal analysis, augmented by on-board temperature monitoring, provides temperatures for each surface of a similar geometric model. This paper describes the physical basis for the simulations, the methodologies, and the predicted migration of the contaminant for various bake-out scenarios and assumptions.

Keywords: X-ray astronomy, CCDs, contamination, modeling and simulation, spacecraft operations

1. INTRODUCTION

Launched on 1999 July 23, the *Chandra X-ray Observatory*^{1, 2, 3} continues to provide superb arcsecond imaging, imaging spectrometry, and high-resolution dispersive spectroscopy of cosmic x-ray sources. Of its two interchangeable focal-plane instruments, the (microchannel-plate) High-Resolution Camera⁴ (HRC) operates at ambient temperature within the Science Instrument Module (SIM); whereas the Advanced CCD Imaging Spectrometer⁵ (ACIS) requires significant cooling to optimize CCD performance. Through passive radiative cooling compensated by electrical heaters, the ACIS instrument holds the CCDs at about -120°C and the camera housing at about -60°C.

The ACIS optical blocking filter (OBF) and camera housing isolate the focal-plane cavity (containing the CCDs) from the rest of the Observatory, venting effectively only to space. However, the outward face of the OBF, the camera top, the inner and outer surfaces of the snoot, and the inner surface of the collimator bound the ACIS cavity (Figure 1, right) that connects to the remainder of the optical cavity (Figure 1, left) through the SIM cavity (Figure 1, right). The large optical cavity vents to space near the end of the long Optical Bench Assembly (OBA) opposite the ACIS. The ACIS surfaces at about -60°C are by far the coldest surfaces within *Chandra*'s optical cavity. Over the six years of operation thus far, these cold surfaces have accumulated a ($\approx 150 \mu\text{g cm}^{-2}$) layer of an unidentified molecular contaminant, with an estimated total mass less than 1 g. Because the ACIS OBF is itself a cold surface, the accumulated contaminant attenuates—most noticeably at low energies—the x-ray flux reaching the ACIS focal plane.⁶

* Contact author SLO: Steve.O'Dell@nasa.gov; phone 1 256-961-7776; fax 1 256-961-7213; wwwastro.msfc.nasa.gov

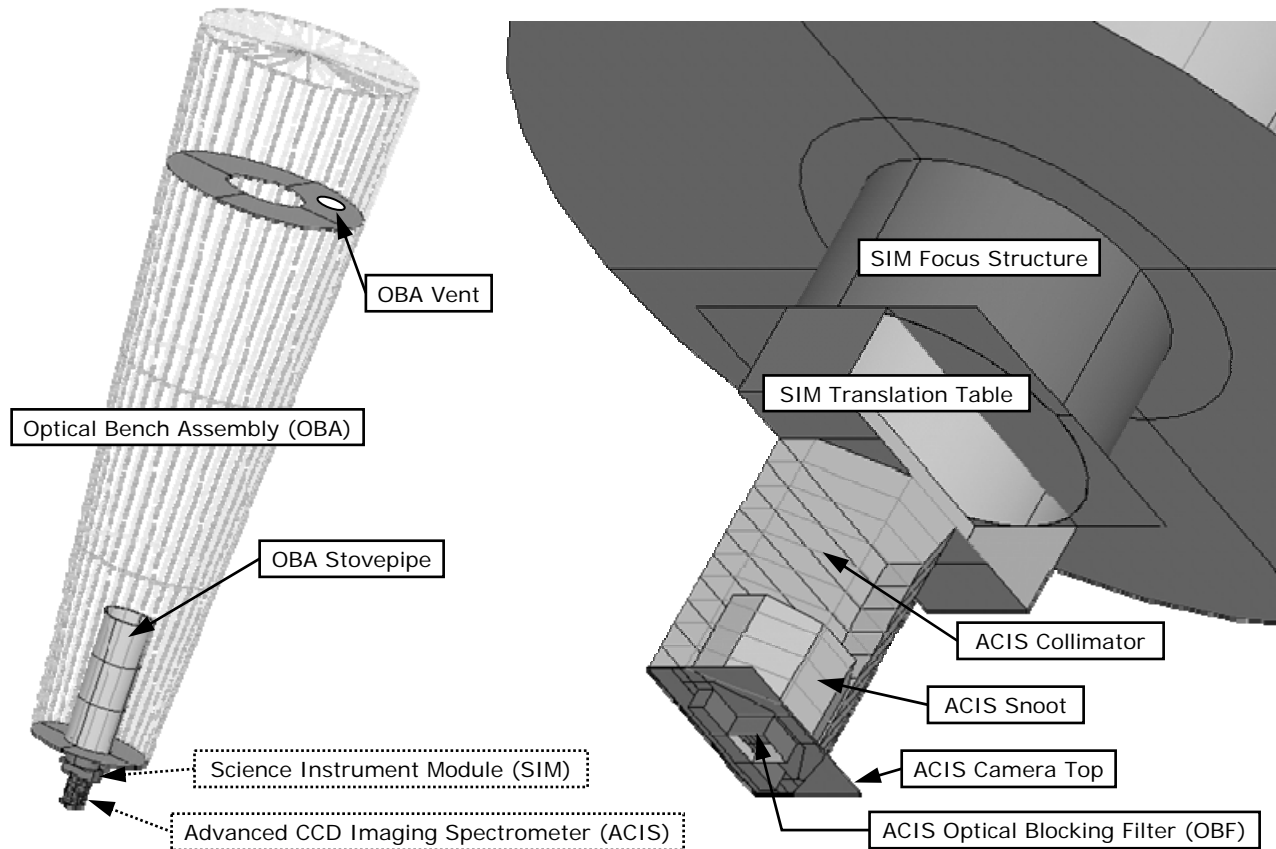


Figure 1: Geometric model for the optical cavity of the *Chandra X-ray Observatory*. The left panel shows the full optical cavity of the Observatory; the right panel, the ACIS and SIM cavities.

Since the discovery in 2002 that contamination on the OBF was accumulating more rapidly than expected, the *Chandra* team has been conducting a detailed investigation of risks, benefits, and efficacy of baking ACIS.⁷ While pre-flight contamination predictions indicated that an on-orbit bake would probably not be necessary, the ACIS team maintained the capability for on-orbit room-temperature bakes. Indeed, the ACIS team executed one such bake early in the mission—in an effort to anneal radiation damage to the front-illuminated CCDs—and conducted dozens of pre-flight bakes. Furthermore, thorough studies by the *Chandra* team found that room-temperature bakes present no credible risk to the ACIS or to the spacecraft. However, contamination-migration simulations indicate that the parameter space for a successful bake is small and that the bake could plausibly result in more contamination on the OBF, thus reducing further the low-energy response of the instrument. Primarily for this reason, the *Chandra* team has postponed for another year any decision on baking the ACIS.

Here we discuss the contamination-migration studies performed as part of the *Chandra* ACIS bake-out investigation. We describe (§2) the modeling methodology, report (§3) some results from the simulations and analytic estimates, and conclude (§4) with a brief summary of results and currently unresolved issues.

2. MODELING METHODOLOGY

In modeling contamination migration throughout the *Chandra* optical cavity, we utilize (§2.1) a realistic physical description of the molecular transport based upon vaporization–deposition dynamics. We employ (§2.2) a medium fidelity geometric model to follow the exchange of the molecular contaminant deposited on surfaces within the optical cavity. Due to the strong temperature dependence of molecular vaporization, we also require (§2.3) thermal analyses of the optical cavity using a geometric model similar to that used to follow the molecular transport.

2.1. Molecular transport

Owing to the very low pressure within the *Chandra* optical cavity, mean free paths are large compared to relevant lengths; thus the transport is molecular—i.e., (line-of-sight) ballistic. Consequently, we developed a simple numerical code for simulating contamination migration. The program evolves the mass column of contaminant at each node according to the (temperature-dependent) vaporization rate from that node and the deposition rate onto that node from material leaving the surfaces of other nodes (plus the same node for concave surfaces). Here, “vaporization” connotes evaporation of a liquid or sublimation of a solid, as appropriate for a given molecular contaminant and temperature.

In order to simulate molecular transport effecting contamination migration, we establish (§2.1.1) transport equations, specify (§2.1.2) relevant constitutive equations, and give (§2.1.3) examples of the material data used in the simulations. The most severe limitation in modeling contamination migration in the *Chandra X-ray Observatory* is that we have not identified the contaminant and thus do not know its material properties. Nonetheless, the modeling provides constraints on the volatility of the contaminant and allows us to compare the relative merits of scenarios for baking the ACIS.

2.1.1. Transport equations

Figure 2 shows relevant parameters for each node—surface area A_j at temperature T_j and mass column μ_j and mass departure rate $\dot{\mu}_j^-$ from the surface. The exchange of material also depends upon the view factor f_{jk} , which specifies the fraction of material leaving node k that impinges upon the surface of node j . These view factors, of course, depend upon the geometry (§2.2) of the optical cavity.

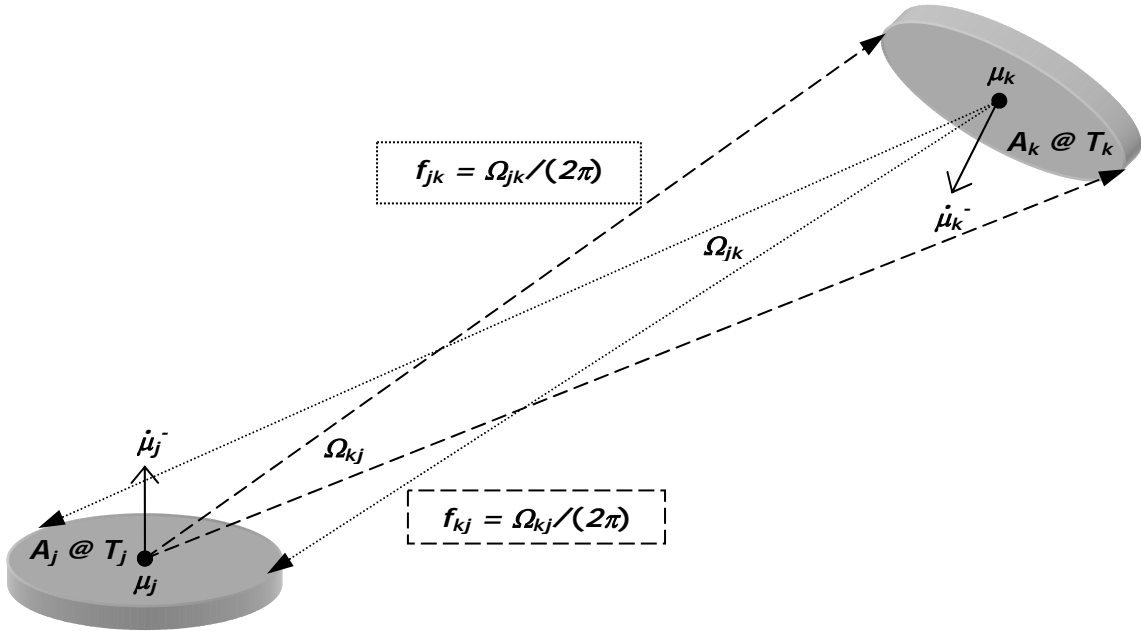


Figure 2: Parameters governing molecular transport of a contaminant. An area A_j and a temperature T_j characterize each node j ; the view factor f_{jk} specifies the fraction of the directional hemisphere occupied by area A_j as viewed from node k . The mass column μ_j and mass departure rate $\dot{\mu}_j^-$ characterize the contaminant on the surface of each node j .

For each node j , the mass column μ_j changes at a rate (Equation 1) determined by the mass arrival rate from all nodes minus the departure rate from the given node. For a vent, the mass departure rate is identically zero. The mass arrival rate $\dot{\mu}_j^+$ at each node is the appropriately (area and view-factor) weighted sum of mass departure rates from all nodes.

Equation 1:
$$\frac{d\mu_j}{dt} = \dot{\mu}_j^+ - \dot{\mu}_j^- = \left(\sum_k \dot{\mu}_k^+ f_{jk} \frac{A_k}{A_j} \right) - \dot{\mu}_j^-.$$

For a contaminated surface, the mass departure rate from a node is the (temperature-dependent) mass vaporization rate from that node (Equation 2). For a clean surface, it is the lesser of the mass vaporization rate from and the mass arrival rate onto that node: Obviously, the mass column μ_j of contaminant cannot become negative. If a given surface is clean and its temperature-dependent vaporization rate exceeds the mass arrival rate onto it, then that surface remains clean and the mass departure rate equals the arrival rate—i.e., Equation 1 goes to zero and the surface remains clean.

$$\text{Equation 2: } \begin{array}{l} \dot{\mu}_j^- = \dot{\mu}_j^+, \mu_j = 0 \quad \& \quad \dot{\mu}_j^+ < \dot{\mu}_v(T_j) \\ \dot{\mu}_j^- = \dot{\mu}_v(T_j), \mu_j > 0 \quad | \quad \dot{\mu}_j^+ > \dot{\mu}_v(T_j). \end{array}$$

The finite-difference equation (Equation 3) used for the numerical simulations more clearly explains Equation 1 and Equation 2. For time interval $\Delta t_n = t_n - t_{n-1}$ at time step n , the mass column μ_j^n at node j is its value at step $n - 1$ incremented by the arriving mass and decremented by the departing mass. Equation 3 explicitly ensures that, for each node, the mass of material vaporized in time step n does not exceed the mass present at the start of that step. In that we track the mass at each node including the vent, the total mass m of contaminant is conserved (Equation 4).

$$\text{Equation 3: } \mu_j^n = \mu_j^{n-1} + \left(\sum_k \min[\dot{\mu}_v(T_k^{n-1})\Delta t_n, \mu_k^{n-1}] f_{jk} \frac{A_k}{A_j} \right) - \min[\dot{\mu}_v(T_j^{n-1})\Delta t_n, \mu_j^{n-1}].$$

$$\text{Equation 4: } m = \sum_j m_j = \sum_j \mu_j A_j.$$

2.1.2. Constitutive equations

In order to integrate numerically the system of transport equations (Equation 3) with time, we need the contaminant's mass vaporization rate as a function of temperature—in addition to geometric parameters (Figure 2, §2.2) and nodal temperatures (§2.3). Evaluating the mass vaporization rate requires the constitutive equation for the temperature dependence and relevant material data (§2.1.3) for a specified contaminant at some reference temperature.

Equation 5 relates the mass (evaporation or sublimation) vaporization rate to the corresponding vapor pressure, the physical parameter typically cited. The mass vaporization rate is a mass flux (mass per area per time), which is simply the vapor pressure (twice a momentum flux) divided by some characteristic speed—namely, $2\langle v^2 \rangle / \langle |v| \rangle$. Therefore, with R the ideal gas constant and M the molar mass,

$$\text{Equation 5: } \dot{\mu}_v(T) = \frac{\langle |v| \rangle}{2\langle v^2 \rangle} P_v(T) = \frac{P_v(T)}{\sqrt{2\pi RT/M}}.$$

For the temperature dependence of the mass vaporization rate, we use the Clausius–Clapeyron equation (Equation 6), which parameterizes the vapor pressure or (through Equation 5) the mass vaporization rate at any temperature T in terms of its value at a reference temperature T_0 and its enthalpy of vaporization (evaporation or sublimation, as appropriate) ΔH . Note the strong—exponential—dependence of volatility upon temperature.

$$\text{Equation 6: } P_v(T) = P_v(T_0) \text{Exp} \left[-\frac{\Delta H}{R} \left(\frac{1}{T} - \frac{1}{T_0} \right) \right]; \quad \dot{\mu}_v(T) = \dot{\mu}_v(T_0) \sqrt{\frac{T_0}{T}} \text{Exp} \left[-\frac{\Delta H}{R} \left(\frac{1}{T} - \frac{1}{T_0} \right) \right].$$

2.1.3. Material data

For simulating contamination migration, relevant material data are molar mass M , vapor pressure $P_v(T_0)$ at reference temperature T_0 , and vaporization enthalpy ΔH (nearly constant with temperature, except at a phase change). Again, “vaporization” here connotes either evaporation of a liquid or sublimation of a solid, as appropriate. If a liquid–solid phase change occurs within the temperature range of interest, we also need the freezing temperature T_{l-s} and the latent heat of fusion—i.e., melting enthalpy, equal to the difference between the sublimation and evaporation enthalpies. The temperature range of interest for simulating contamination migration in the *Chandra* optical cavity is (-65°C , $+30^\circ\text{C}$) = (208 K, 303 K); the reference temperature for relevant material data^{8, 9, 10, 11, 12} is $+20^\circ\text{C} = 293$ K.

Unfortunately, we have not identified the molecular contaminant on the ACIS OBF. Analysis¹³ of high-resolution spectroscopy of celestial sources using ACIS with *Chandra's* objective transmission gratings—especially, the Low-Energy Transmission Grating¹⁴ (LETG)—has shown that the contamination is primarily aliphatic (single-bonded) carbon, with some oxygen ($N_O \approx N_C/11$) and fluorine ($N_F \approx N_C/15$) but little nitrogen ($N_N < N_C/30$). However, the x-ray data cannot measure the molecular weight of the contaminant(s), which is important to estimating volatility.

Figure 3 shows the mass vaporization rates of several organic compounds over the temperature range of interest. In most simulation cases, we scale the volatility over this temperature range to that of dioctyl phthalate (DOP, a liquid) or to that of docosane (a solid). We use these two organic compounds as references because each has a mass vaporization rate of about $5 \times 10^{-3} \mu\text{g cm}^{-2} \text{s}^{-1}$ at $+20^\circ\text{C}$. This is approximately the minimum volatility for a room-temperature bake to clean the OBF in one orbit. Later (§3.3), we shall briefly address the constraints displayed in Figure 3. Note that for similar room-temperature volatilities, the vaporization of a solid (by sublimation) is even more sensitive to temperature than that of a liquid (by evaporation): With its exponential dependence upon temperature (Equation 6), the near-room-temperature volatility of relevant materials doubles every $+3^\circ\text{C}$ for solids or every $+5^\circ\text{C}$ for liquids.

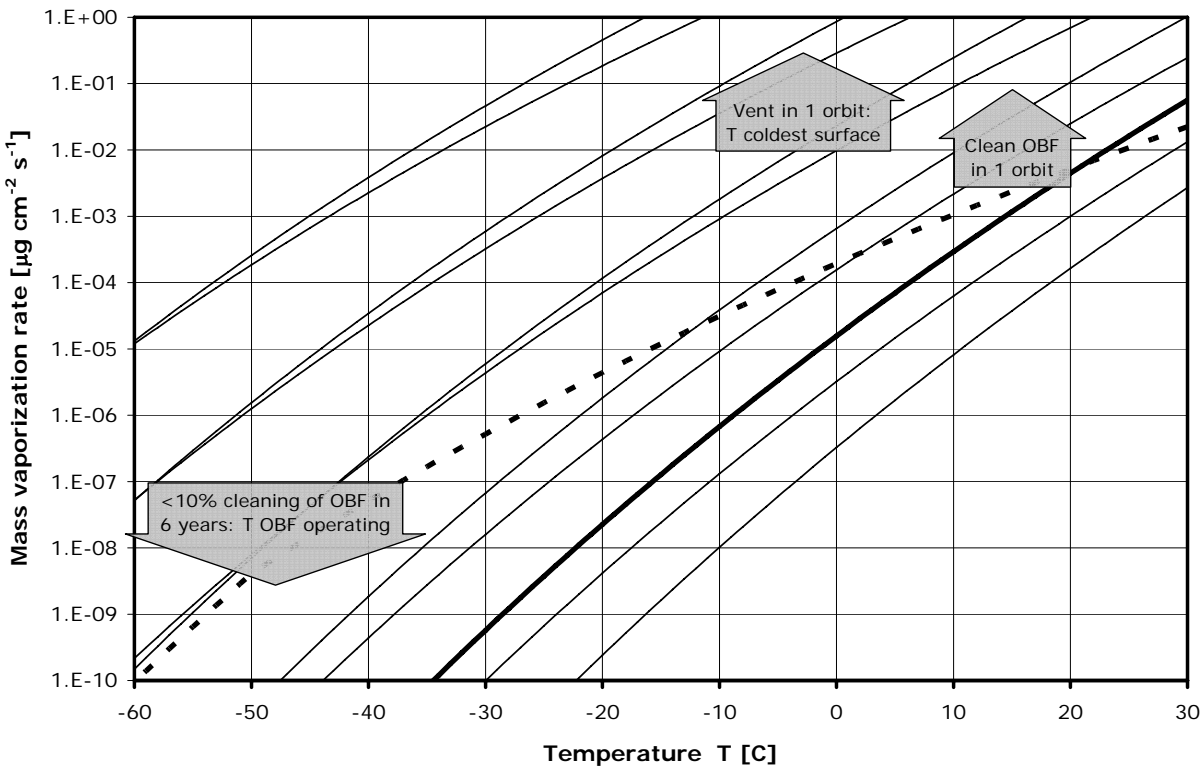


Figure 3: Mass vaporization rates of some organic compounds, compared with constraints on volatility of the contaminant on the ACIS optical blocking filter. The thick dashed line denotes dioctyl phthalate (DOP, $\text{C}_{24}\text{H}_{38}\text{O}_4$); the thick solid line, docosane ($\text{C}_{22}\text{H}_{46}$); and the thin solid lines, other alkanes from tetradecane ($\text{C}_{14}\text{H}_{30}$, most volatile) to tetracosane ($\text{C}_{24}\text{H}_{50}$, least volatile). Note the flatter temperature dependence of DOP, which is a liquid down to -50°C : The displayed alkanes are solid throughout the temperature range shown.

2.2. Geometric model

For the contamination-migration simulations, we started with a geometric model developed by the spacecraft prime contractor—TRW Space Technologies (now Northrop–Grumman, or NGST)—for its thermal analysis of the *Chandra X-ray Observatory*. In regions of the optical cavity subject to strong temperature gradients (e.g., the ACIS collimator) or otherwise of special interest (e.g., the OBF), we resolved nodes into finer nodes to improve resolution. The resulting model contains 224 nodes with a total area of nearly 70 m^2 . Table 1 lists summary data for this model, grouping the 224 nodes into the 9 geometric elements identified in Figure 1. The three columns of representative temperatures are rough

averages over nodes comprising each element for normal operations and for baking with abort heaters “off” and “on” (see §3) . For the simulations, we assign each node a temperature based upon detailed thermal analyses (§2.3).

Table 1: Properties of the geometric model for the *Chandra* optical cavity.

Geometric element Name	Nodes [#]	Area [cm ²]	Representative T [°C]		
			Ops	AH off	AH on
ACIS Optical Blocking Filter (OBF)	36	68	-50	+20	+20
ACIS Camera Top	32	244	-60	+20	+20
ACIS Snoot (inner + outer surfaces)	12	1335	-60	+21	+21
ACIS Collimator	60	2416	-40	+5	+16
SIM Translation Table	10	1814	-10	-9	+10
SIM Focus Structure	4	2839	+4	+5	+5
OBA Stovepipe	24	54096	+10	+10	+10
Optical Bench Assembly (OBA)	41	634688	+12	+12	+12
OBA Vent	5	476			
Total	224	697976			

In addition to the area A_j and temperature T_j of each node, solving the system of transport equations (Equation 3) requires a value for each view factor (Figure 2) f_{jk} . Recognizing that these are precisely the same set of parameters involved in the thermal analysis (§2.3), we used the geometry output of the Thermal Radiative Analysis System¹⁵ (TRASYS) computer analysis of the *Chandra* optical cavity (Figure 1) as input parameters for the contamination-migration simulations. For computational efficiency, the TRASYS output does not report view factors less than a small user-defined value. Therefore, we renormalized the view factors to ensure that $\sum_j f_{jk} = 1$. Not renormalizing the view factors would cause a computational leak¹⁶ that would artificially lose mass from the system. Because we track the mass on all nodes *including vents*, the total mass must be conserved throughout the simulation (Equation 4).

2.3. Thermal analyses

We performed several thermal analyses of the *Chandra X-ray Observatory*, with special attention to temperatures within the ACIS cavity. As prime contractor, NGST performed the overall thermal analysis of the Observatory (§2.3.1). As ACIS integrator, Lockheed–Martin performed finer resolution thermal analyses of the ACIS cavity (§2.3.2). These thermal analyses employ TRASYS or comparable software using geometric models similar to that described above (Figure 1 and §2.2). Typically, the estimated uncertainty in the thermal-model temperatures is 3–5°C, less for nodes conductively coupled to temperature-controlled surfaces.

2.3.1. Observatory temperatures

By comparing the thermal-model predictions with telemetry of on-board thermocouple readings, NGST has checked the accuracy of its static and transient thermal analyses. On-board thermostats control heaters that hold thermal zones of the cold-biased optical cavity at their respective set points. Consequently, temperatures within the rest of the optical cavity are essentially independent of those within the ACIS cavity. Furthermore, apart from the SIM and ACIS cavities, temperatures within the optical cavity are relatively warm—(+10°C, +21°C). Hence, these surfaces, comprising about 99% of the optical-cavity surface area (Table 1), never accumulate molecular contamination: Equation 1 is identically zero for the nodes of these warm surfaces—i.e., contaminant molecules effectively just bounce off such surfaces.

On the other hand, during a room-temperature bake of the ACIS instrument, the SIM cavity is the coldest region within the optical cavity. At about -10°C (“AH off” of Table 1), the SIM translation table becomes the cryo-getter for the entire optical cavity during a bake of the ACIS. Our simulations (§3.2), as well as analytic estimates (see constraint on Figure 3 and in §3.3), demonstrated that the translation table severely retards total venting from the optical cavity. For this reason, the *Chandra* team investigated the possibility of using “abort heaters” on the SIM. The contingency application of these heaters was to support a mission aborted prior to deployment, in which case the space-shuttle

orbiter would have returned with Chandra aboard. NGST thermal analyses indicated that use of the abort heaters would raise the temperature of SIM translation table to about +10°C (“AH on” of Table 1), making the SIM focus structure the optical cavity’s cryo getter at about +5°C. As anticipated and predicted by analytic estimates, our contamination-migration simulations showed that use of the abort heaters would help promote venting.

Ultimately, the *Chandra* team decided not to use the abort heaters. Not designed for use after deployment, some of abort-heater wiring is exposed to the space environment. Thus, concern about radiation and thermal-mechanical degradation of the wiring’s insulation precludes use of the abort heaters. However, the abort heaters are not necessary for a successful bake. Our simulations (§3.2), as well as analytic estimates, showed that the cold (-10°C) SIM translation table actually promotes cleaning of the OBF during the bake and could cryo-trap plausible contaminants for perhaps years.

2.3.2. ACIS temperatures

The clear criterion for a successful bake is cleaning the molecular contaminant from the ACIS OBF. The ACIS cavity has likely trapped most of the low-volatility molecular contaminants in the *Chandra* optical cavity. Furthermore, it experiences the largest temperature change between normal operations ($\approx -60^\circ\text{C}$) and baking conditions ($\approx +20^\circ\text{C}$) and also exhibits the strongest temperature gradients (Figure 4). Thus, Lockheed–Martin performed a rather high-resolution thermal analysis for the ACIS cavity (Figure 4), with even finer granularity for the OBF (Figure 5 and Figure 6).

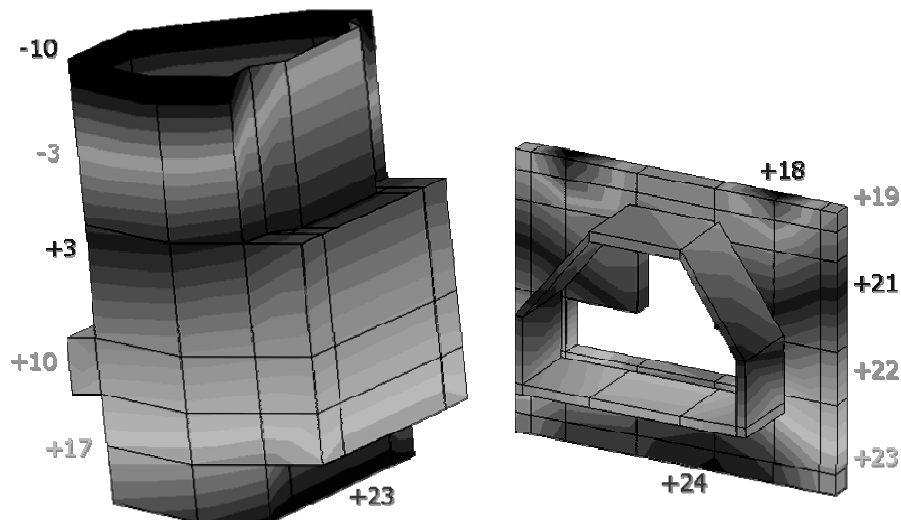


Figure 4: Model temperature distributions for the ACIS under nominal baking conditions, with SIM abort heaters “off”. The left panel displays the collimator; the right panel, the camera top and snoot (located at the bottom of the collimator).

It is unavoidable and unfortunate that the temperature of the most critical surface—i.e., the OBF—cannot be directly controlled or monitored. The thermal coupling of the OBF is primarily radiative to the ACIS cavity above and to the CCD focal plane below. Therefore, the temperature of the OBF is sensitive to the thermal emissivity on its top and bottom faces. An important realization in the thermal analysis of the ACIS cavity is that the emissivity of a contaminated surface can be substantially higher than that of a pristine metallic surface, depending upon the thickness of the molecular film. The thermal emissivity of the pristine aluminized polyimide OBF (and of other metallic surfaces in the ACIS cavity) is small—namely, $\epsilon \approx 0.05$. However, for the mass column ($\approx 150 \mu\text{g cm}^{-2}$) of contaminant on the OBF and other cold surfaces, the emissivity could be substantially larger—e.g., $\epsilon \approx 0.30$. Consequently, Lockheed–Martin ran thermal analyses for $\epsilon \approx 0.05$ and for $\epsilon \approx 0.30$ on normally cold surfaces that probably are contaminated at a level comparable to that on the OBF. For normal (cold) operations (Figure 5), the predicted temperature at the center of the OBF is about 16°C warmer for $\epsilon \approx 0.30$ than for $\epsilon \approx 0.05$; for bake conditions, about 4°C colder (Figure 6). As we shall see (§3), these temperature differences and the inherent uncertainty in the temperature predictions significantly influence our assessment of potential efficacy and risk in baking the ACIS (§4).

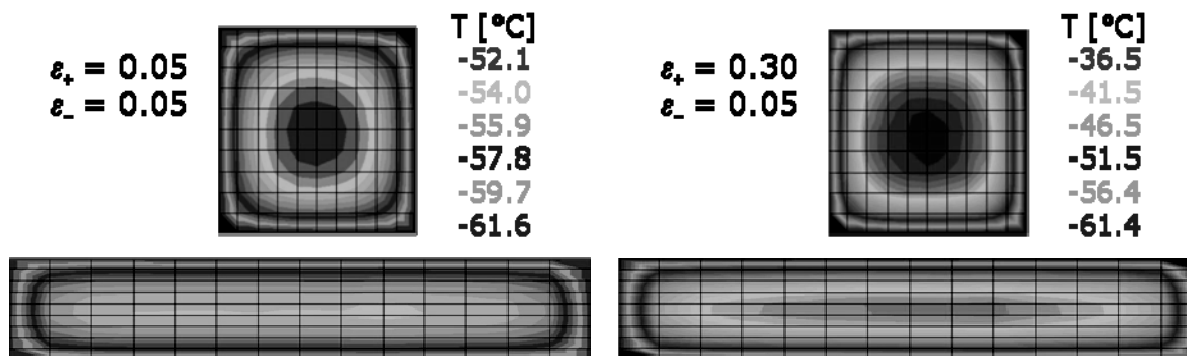


Figure 5: Model temperatures of the ACIS OBF during normal operations, with the focal plane at -120°C and camera-housing heater set to -60°C . Left panel shows the temperature distribution for a pristine surface or for a low-emissivity contaminant; right, for a high-emissivity contaminant. The presence of a thick contaminating layer on the outward surface of the OBF can change the temperature at the OBF's center by about $+16^{\circ}\text{C}$ during normal operations.

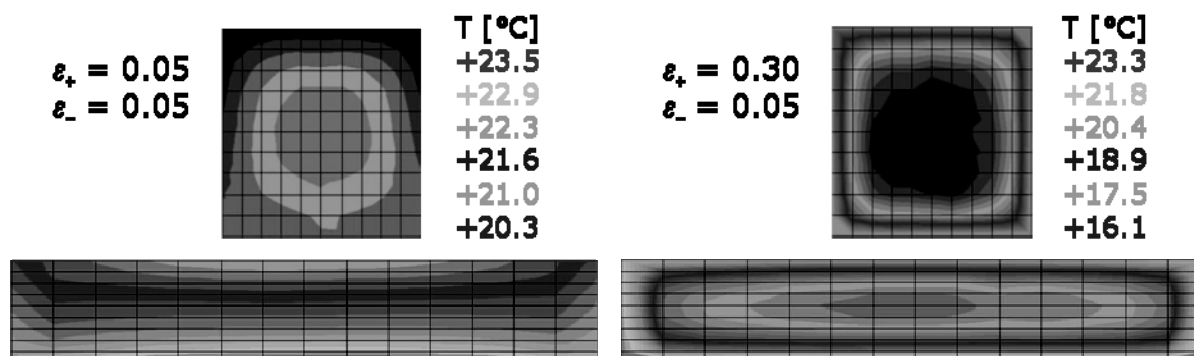


Figure 6: Model temperatures of the ACIS OBF during a warm bake, with the focal plane at $+30^{\circ}\text{C}$ and camera-housing heater set to $+20^{\circ}\text{C}$. Left panel shows the temperature distribution for a pristine surface or for a low-emissivity contaminant; right, for a high-emissivity contaminant. The presence of a thick contaminating layer on the outward surface of the OBF can change the temperature at the OBF's center by about -4°C during a warm bake.

3. SIMULATION CASES

During the course of the ACIS bake-out investigation, we have run numerous contamination-migration simulations for various scenarios. Because the contaminant's volatility is unidentified and the temperatures are uncertain, we have necessarily explored a substantial volume of parameter space through simulations, scaling, and analytic estimates. Here we present some examples of the results of the simulations, both (§3.1) for the pre-bake deposition and (§3.2) for the bake and subsequent re-deposition. In addition, we briefly discuss (§3.3) constraints on the contaminant's volatility.

3.1. Pre-bake deposition

We start the simulation of pre-bake deposition with the contaminant on a warm surface outside the ACIS cavity. The simulation follows the contaminant as it migrates via vaporization (sublimation for solids; evaporation for liquids) and deposition toward the colder surfaces at the bottom of the ACIS cavity and toward the vent to space. After simulating several years of deposition, we stop the simulation and scale the average mass column on the OBF to the value observed. Because we have not identified the contaminant, we have simulated cases for various contaminants having volatilities consistent with reasonable constraints (Figure 3 and §3.3).

Figure 7 illustrates a case simulating the pre-bake deposition of docosane ($\text{C}_{22}\text{H}_{44}$, solid below $+43^{\circ}\text{C} = 316\text{ K}$) onto the ACIS instrument. Because of its very low volatility at the OBF operating temperature, contaminant molecules

impinging on the OBF remain there. Thus, the distribution of mass column μ on a cold surfaces such as the OBF is simply the temporal integral of the mass arrival rate $\dot{\mu}^+$ (§2.1.1) onto that surface. We refer to this distribution as “deposition dominated” or “view-factor dominated” because the view factors to warmer contaminated surfaces, which are still vaporizing, govern the distribution.

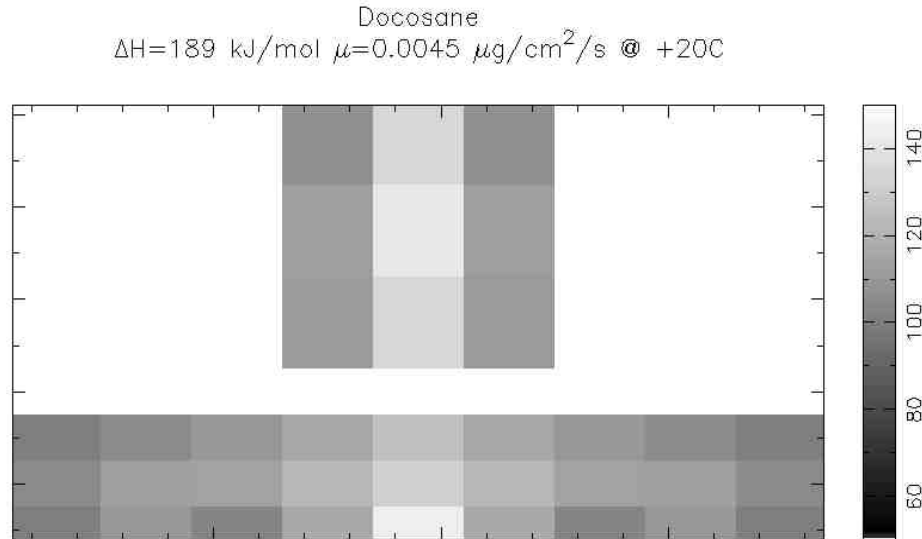


Figure 7: Deposition simulation of a contaminant onto the ACIS optical blocking filter (OBF). OBF-I (top) covers the 2×2-CCD imaging array; OBF-S (bottom), the 6×1-CCD spectroscopy array. The gray scale indicates the mass column μ (in $\mu\text{g cm}^{-2}$) of contaminant on the OBF.

As Figure 7 illustrates, a distribution that is dominated by (deposition) view factor should be thicker near the center of an OBF than near its edges, at least for the geometric model used. However, the observed distribution shows the opposite gradient.¹⁷ In contrast, a distribution dominated by (temperature-dependent) vaporization would be thinner near the center because the thermal models predict that an OBF is warmer near its center during normal operations. However, the x-ray data show that the contaminant’s mass column continues to increase with time, uniformly over an OBF. Were the distribution vaporization-dominated and the predicted temperature gradients were correct, we would expect the center of an OBF to be cleaning much faster than the edges. Thus the model does not simulate the fine-scale mass-column distribution on the OBF. Neglected physical effects—such as surface migration or polymerization—might help explain the observed distribution. Nonetheless, this discrepancy remains an issue that we have not resolved.

3.2. Bake and re-deposition

The empirically scaled contaminant distribution of the pre-bake deposition simulation (§3.1) then serves as the initial distribution for simulating the bake and subsequent re-deposition. Contamination-migration simulations and analytic estimates for numerous bake scenarios led to two rather obvious conclusions:

1. To maximize the likelihood of cleaning the OBF, the bake should be as warm and as long as feasible.
2. To preclude additional accumulation on the OBF, the OBF should be the warmest surface in the ACIS cavity.

Consideration of these objectives, ACIS bake experience, and the need to hide ACIS during radiation-belt passes gave rise to a standard 1-orbit warm-bake scenario. The ACIS focal-plane temperature ramps from -120°C to $+30^{\circ}\text{C}$ over 5 hours, holds for 44 hours (158 ks), and returns to -120°C over 14 hours. When the focal plane is warm, the camera-housing set point rises from -60°C to $+20^{\circ}\text{C}$ and returns to -60°C before the focal plane cools. We follow subsequent re-deposition for 6.3 y (2×10^8 s), keeping the ACIS in the observing position to ease computational complexity.

Lacking identification of the contaminant, we performed most contamination-migration simulations either for dioctyl phthalate or for docosane. As explained earlier (§2.1.3), these materials each have about the minimum volatility at

+20°C for the standard 1-orbit warm bake to clean the OBF (Figure 3). However, the temperature sensitivity of the solid docosane is greater than that of liquid dioctyl phthalate. The standard bake would easily clean much higher volatility contaminants from the OBF, but could not clean much lower volatility ones.

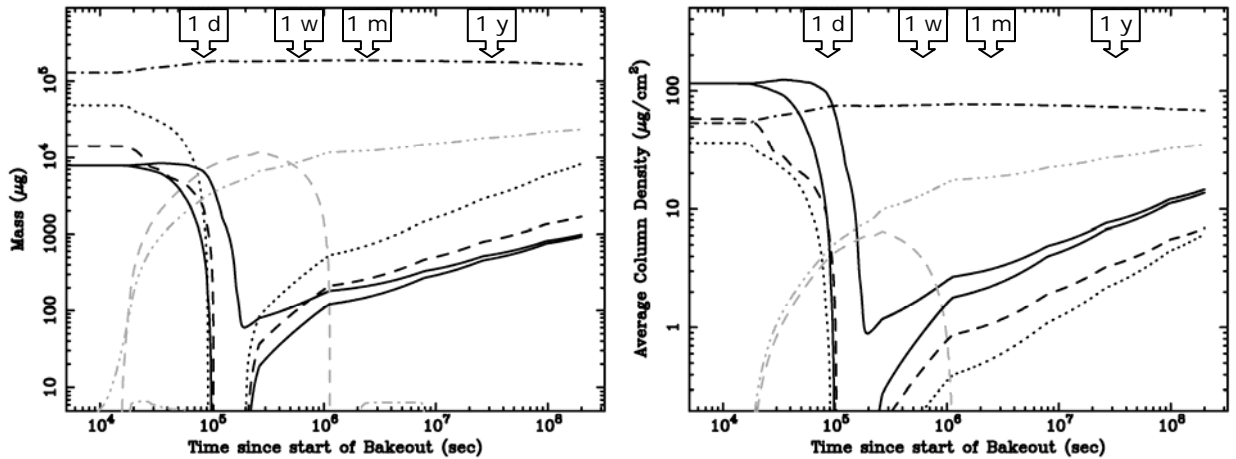


Figure 8: Simulation of bake and re-deposition of dioctyl phthalate (liquid), for a thermal model based upon a low-emissivity ($\epsilon = 0.05$) contaminating layer. Left panel gives the mass of contaminant; right panel, its average mass column. Black lines denote ACIS OBF (solid), camera top (dashed), snoot (dotted), and collimator (dot-dashed); gray lines denote SIM translation table (dashed) and focus structure (dotted) and optical-cavity vent (triple-dot-dashed). The two solid lines for the OBF represent the nominal thermal case and a de-rated case with the OBF center 5°C below nominal.

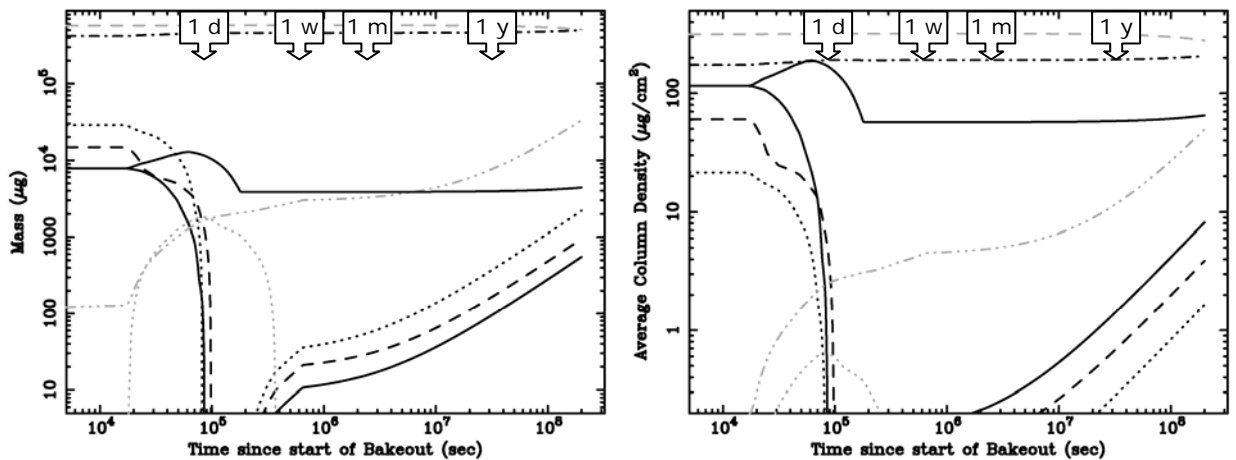


Figure 9: Simulation of bake and re-deposition of docosane (solid), for a thermal model based upon a low-emissivity ($\epsilon = 0.05$) contaminating layer. See caption for Figure 8.

Figure 8 and Figure 9 track the evolution of mass and average mass column on geometric elements of the optical cavity (Figure 1 and Table 1) for dioctyl phthalate and for docosane, respectively. Assumed nominal temperatures are from a thermal model that uses an emissivity $\epsilon = 0.05$ on both faces of the OBF. In each plot, the higher curve for the OBF corresponds to (-5°C) de-rated temperatures on the OBF. By construction—i.e., selection of reference contaminant—the standard bake at nominal temperatures cleans the OBF. For de-rated OBF temperatures, the standard bake is more effective removing the liquid than the solid contaminant. Although venting is incomplete, re-deposition requires years.

Figure 10 also tracks the evolution for docosane, but assumes temperatures from a thermal model that uses an emissivity $\epsilon = 0.30$ on the OBF's outward face and on other contaminated surfaces. The lower temperature at the OBF's center

prevents complete cleaning for either nominal or de-rated OBF temperatures. Of greater concern, however, is the prediction for the de-rated case: The OBF could be more contaminated after than before the bake. Clearly, this is an unacceptable end state, the possibility of which has dampened our enthusiasm for baking ACIS at this time.

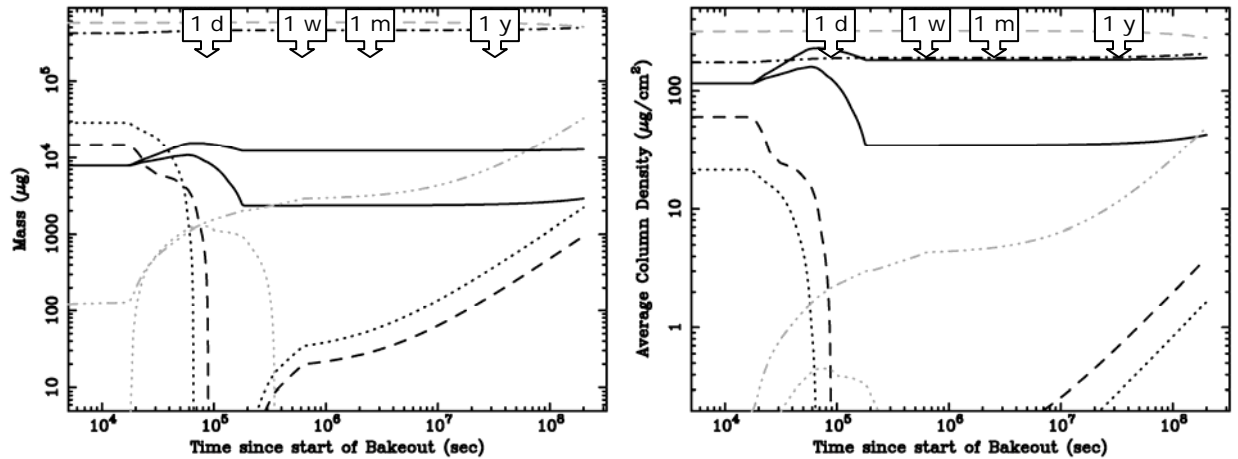


Figure 10: Simulation of bake and re-deposition of docosane, for a thermal model based upon a high-emissivity ($\epsilon = 0.30$) contaminating layer. See caption for Figure 8.

3.3. Constraints on volatility

Figure 3 displays three constraints on the volatility of the unidentified contaminant on the OBF.

1. The constancy of the mass-column gradient across the OBF suggests that $< 10\%$ of the contaminant has vaporized in 6 years. Thus, the mass vaporization rate $< 1 \times 10^{-7} \mu\text{g cm}^{-2} \text{s}^{-1}$ at the operating temperature at the OBF's center.
2. In order to vent all the contaminant in a 1-orbit bake, the mass vaporization rate $> 1 \times 10^{-2} \mu\text{g cm}^{-2} \text{s}^{-1}$ at the temperature of the coldest surface during the bake—with abort heaters off, the SIM translation table at -10°C .
3. In order to clean the contaminant from the OBF in a 1-orbit bake, the mass vaporization rate $> 3 \times 10^{-3} \mu\text{g cm}^{-2} \text{s}^{-1}$ at the baking temperature of the OBF's center.

Because the OBF has not cleaned in 6 years of operation, the parameter space for the standard bake to vent totally the contaminant is essentially zero. The parameter space for it to clean the OBF is small if the contaminant is liquid and somewhat larger if it is solid. A high-emissivity contaminated OBF (§2.3.2) is (16°C) warmer during operations and (4°C) cooler during bake than the pristine OBF: This dramatically shrinks the parameter space for a successful bake.

4. SUMMARY AND ISSUES

In summary, we have developed a contamination-migration model for the *Chandra X-ray Observatory*. We have used it to simulate deposition, baking, and re-deposition of molecular contamination within the *Chandra* optical cavity. The model has served as a useful tool in assessing the relative merits and efficacy of various scenarios for cleaning the contaminant from the ACIS optical blocking filter (OBF).

Currently, the utility of this tool for high-fidelity absolute predictions is limited. First, absolute predictions require knowledge of the volatility of the contaminant, which we still have not identified. Second, uncertainties in temperatures—exacerbated by the dependence of thermal emissivity upon contaminant thickness—propagate exponentially to the rate error. Third, the fine-scale fidelity of the model—especially, in predicting the mass-column gradient across the OBF—is inadequate: Thus, we may be missing important physics or need finer scale geometry.

Despite these limitations, the contamination-migration simulations and analytic estimates have effectively guided evaluation of strategies for baking ACIS. For example, these analyses have shown the following:

1. Use of abort heaters promotes more rapid venting. (However, a risk assessment precludes use of these heaters.)

2. Total venting is unnecessary to clean the OBF during a bake and the re-deposition time scale could be years.
3. Baking the ACIS cavity will not increase the mass column on the OBF if it is the warmest surface during the bake.
4. Warmer operating temperatures resulting from higher-emissivity contaminated surfaces shrink the parameter space for a successful bake.
5. Colder baking temperatures resulting from higher-emissivity contaminated surfaces could result in more contamination on the OBF after than before the bake.

REFERENCES

-
- ¹ M.C. Weisskopf, T.L. Aldcroft, M. Bautz, R.A. Cameron, D. Dewey, J.J. Drake, C.E. Grant, H.L. Marshall, & S.S. Murray, "An Overview of the Performance of the Chandra X-ray Observatory", *Exp. Astron.*, **16**, 1–68, 2003.
 - ² M.C. Weisskopf, B. Brinkman, C. Canizares, G. Garmire, S. Murray, & L.P. Van Speybroeck, "An Overview of the Performance and Scientific Results from the Chandra X-Ray Observatory", *Pub. Astron. Soc. Pacific*, **114**, 1–24, 2002.
 - ³ M.C. Weisskopf, H.D. Tananbaum, L.P. Van Speybroeck, & S.L. O'Dell, "Chandra X-ray Observatory (CXO): overview", *Proc. SPIE*, **4012**, 2–16, 2000.
 - ⁴ S.S. Murray, G.K. Austin, J.H. Chappell, J.J. Gomes, A.T. Kenter, R.P. Kraft, G.R. Meehan, M.V. Zombeck, G.W. Fraser, & S. Serio, "In-flight performance of the Chandra High-Resolution Camera", *Proc. SPIE*, **4012**, 68–80, 2000.
 - ⁵ G.P. Garmire, M.W. Bautz, P.G. Ford, J.A. Nousek, & G.R. Ricker Jr., "Advanced CCD Imaging Spectrometer (ACIS) instrument on the Chandra X-ray Observatory", *Proc. SPIE*, **4851**, 28–44, 2003.
 - ⁶ P.P. Plucinsky, N.S. Schulz, H.L. Marshall, C.E. Grant, G. Chartas, D. Sanwal, M. Teter, A.A. Vikhlinin, R.J. Edgar, M.W. Wise, G.E. Allen, S.N. Virani, J.M. DePasquale, & M.T. Raley, "Flight spectral response of the ACIS instrument", *Proc. SPIE*, **4851**, 89–100, 2003.
 - ⁷ P.P. Plucinsky, S.L. O'Dell, N.W. Tice, D.A. Swartz, M.W. Bautz, J.M. DePasquale, R.J. Edgar, G.P. Garmire, R. Giordano, C.E. Grant, P. Knollenberg, S. Kissel, B. LaMarr, R. Logan, M. Mach, H.L. Marshall, L. McKendrick, G.Y. Prigozhin, D.A. Schwartz, N.S. Schulz, D. Shropshire, T. Trinh, A.A. Vikhlinin, & S.N. Virani, "An evaluation of a bake-out of the ACIS instrument on the Chandra X-Ray Observatory", *Proc. SPIE*, **5488**, 251–263, 2004.
 - ⁸ J.S. Chickos & W. Hanshaw, "Vapor pressures and vaporization enthalpies of the n-alkanes from C₂₁ to C₃₀ at T = 298.15 K by correlation gas chromatography", *J. Chem. Eng. Data*, **49**, 77–85, 2004.
 - ⁹ A.K. Ray, E.J. Davis, & P. Ravindran, "Determination of ultra-low vapor pressures by submicron droplet evaporation", *J. Chem. Phys.*, **71**, 582–587, 1979.
 - ¹⁰ J.S. Chickos & W.E. Acree Jr., "Enthalpies of sublimation of organic and organometallic compounds, 1910–2001", *J. Phys. Chem. Ref. Data*, **31**, 537–698, 2002.
 - ¹¹ J.S. Chickos & W.E. Acree Jr., "Enthalpies of vaporization of organic and organometallic compounds, 1880–2002", *J. Phys. Chem. Ref. Data*, **32**, 519–878, 2003.
 - ¹² NIST Thermodynamics Research Center, "Vapor Pressure Database", NIST Standard Reference Database 87, 2001.
 - ¹³ H.L. Marshall, A.F. Tennant, C.E. Grant, A.P. Hitchcock, S.L. O'Dell, & P.P. Plucinsky, "Composition of the Chandra ACIS contaminant", *Proc. SPIE*, **5165**, 497–508, 2004.
 - ¹⁴ B.C. Brinkman, T. Gusing, J.S. Kaastra, R. van der Meer, R. Mewe, F.B. Paerels, T. Raassen, J. van Rooijen, H.W. Braeuninger, V. Burwitz, G.D. Hartner, G. Kettenring, P. Predehl, J.J. Drake, C.O. Johnson, A.T. Kenter, R.P. Kraft, S.S. Murray, P.W. Ratzlaff, & B.J. Wargelin, *Proc. SPIE*, **4012**, 81–90, 2000.
 - ¹⁵ R.A. Vogt, "Recent developments in Thermal Radiation Analysis System", in *Computational Aspects of Heat Transfer in Structures* (NASA SEE N82-23473 14-34), 234–251, 1980.
 - ¹⁶ G.T. Tsuyuki, "TRASYS form factor matrix normalization", in *Fourth Annual Thermal and Fluids Analysis Workshop* (NASA SEE N93-13385 03-34), 71–82, 1992.
 - ¹⁷ J.M. DePasquale, P.P. Plucinsky, A.A. Vikhlinin, H.L. Marshall, N.S. Schulz, & R.J. Edgar, "Verifying the ACIS contamination model with 1E0102.2-7219", *Proc. SPIE*, **5501**, 328–338, 2004.